

DenoiseGS: Gaussian Reconstruction Model for Burst Denoising

Yongsen Cheng^{*,1}, Yuanhao Cai^{*,2}, Yulun Zhang^{†,1}

¹ Shanghai Jiao Tong University, ² Johns Hopkins University

Abstract

Burst denoising methods are crucial for enhancing images captured on handheld devices, but they often struggle with large motion or suffer from prohibitive computational costs. In this paper, we propose DenoiseGS, the first framework to leverage the efficiency of 3D Gaussian Splatting for burst denoising. Our approach addresses two key challenges when applying feedforward Gaussian reconstruction model to noisy inputs: the degradation of Gaussian point clouds and the loss of fine details. To this end, we propose a Gaussian self-consistency (GSC) loss, which regularizes the geometry predicted from noisy inputs with high-quality Gaussian point clouds. These point clouds are generated from clean inputs by the same model that we are training, thereby alleviating potential bias or domain gaps. Additionally, we introduce a log-weighted frequency (LWF) loss to strengthen supervision within the spectral domain, effectively preserving fine-grained details. The LWF loss adaptively weights frequency discrepancies in a logarithmic manner, emphasizing challenging high-frequency details. Extensive experiments demonstrate that DenoiseGS significantly exceeds the state-of-the-art NeRF-based methods on both burst denoising and novel view synthesis under noisy conditions, while achieving $250\times$ faster inference speed. Code and models are released at <https://github.com/yscheng04/DenoiseGS>.

1. Introduction

With the growing popularity of smartphones, casual photography has become ubiquitous. However, images captured by handheld devices often suffer from noise due to limited sensor size and challenging imaging conditions. Image denoising, therefore, plays a crucial role in restoring clean results. Among existing approaches, burst denoising, which leverages multiple short-exposure frames, has proven particularly effective. It can exploit inter-frame redundancy to recover details that are lost in single-frame denoising. Nevertheless, burst denoising remains challenging because of complex motion and misalignment across frames.

^{*}Equal Contribution. [†] Corresponding Author: Yulun Zhang.

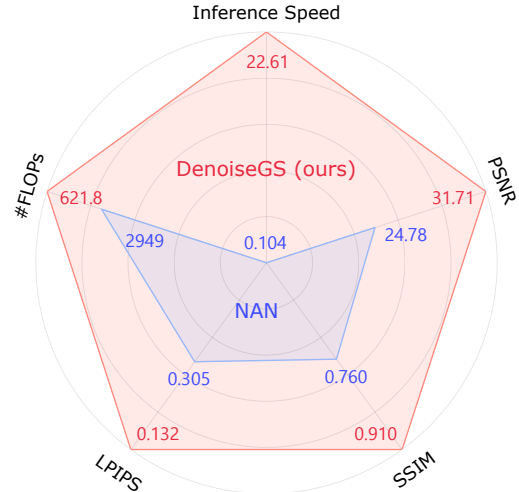


Figure 1. DenoiseGS *vs.* NAN [33]. Our DenoiseGS achieves better PSNR, SSIM, LPIPS values with less FLOPs (in GFLOPs) and faster inference speed (in FPS).

Traditional 2D burst denoising methods [3, 12, 41] typically rely on accurate frame alignment or optical flow estimation, which can easily fail under large motion. On the other hand, modern 3D modeling approaches, exemplified by Neural Radiance Fields (NeRF) [30] offers a more geometrically consistent solution by modeling the 3D structure of a scene. Compared with traditional 2D methods, NeRF-based approaches inherently handle complex parallax and large camera motions, allowing multi-view information to be fused in a physically consistent manner. Leveraging this advantage, Noise-Aware NeRFs (NAN) [33] introduces NeRF into burst denoising. By extending the IBNet [39] with noise-aware components, NAN [33] achieves impressive denoising performance under challenging motions and heavy noise. However, NeRF relies on computationally expensive volume rendering, leading to slow inference speed. For instance, NAN takes 9.6s to denoise a single image at the resolution of 256×256 . This drawback makes it difficult to apply NeRF-based models to practical restoration tasks.

The recent advent of 3D Gaussian Splatting (3DGS) [19] offers a high-speed solution for efficiently tackling 3D reconstruction and NVS challenges. While vanilla 3DGS requires per-scene optimization, feed-forward Gaussian models [7, 8, 49] have enabled efficient inference without test-

time fitting. For example, GS-LRM [49], one of these SOTA feed-forward Gaussian reconstruction models, can efficiently produce novel views in less than 0.1s with as few as 2 input images. The efficiency of these feed-forward methods makes them a promising solution to burst denoising under large motions and high noise levels. However, directly applying these feedforward 3DGS models to burst denoising may encounter two key issues. **First**, they struggle to generate high-quality Gaussian point clouds from noisy inputs. **Second**, fine details are often lost in the rendered results, especially under high noise levels.

To address the above problems, we propose DenoiseGS, an efficient framework for burst denoising built on GS-LRM [49]. Our framework adopts two key components designed to enhance both the spatial structure of reconstructed Gaussian point clouds and the detail preservation of rendered images. **First**, the Gaussian self-consistency (GSC) loss regularizes the geometry with model’s own predictions. During training, we additionally feed clean image bursts into the model to generate Gaussian point clouds with higher quality. The generated Gaussian point clouds can then serve as high-quality 3D guidance. **Second**, the log-weighted frequency (LWF) loss complements spatial supervision with frequency-domain constraints. The LWF loss adaptively weights frequency discrepancies in a logarithmic manner. This design emphasizes challenging high-frequency signals, encouraging the model to better preserve fine details. Extensive experiments demonstrate that our approach enhances GS-LRM [49] without introducing extra overhead and significantly surpasses SOTA burst denoising methods, while achieving faster inference. We also extend our model to novel view synthesis task under noisy conditions, reaching SOTA performance. Overall, the main contributions of our work are outlined below:

- We propose a novel framework, DenoiseGS, for burst denoising. To the best of our knowledge, this paper is the first to introduce 3D Gaussian splatting into the task of burst denoising.
- We design a Gaussian self-consistency (GSC) loss that exploits the model’s inherent ability to produce high-quality Gaussian point clouds from clean input to enhance the quality of point clouds reconstructed from noisy ones.
- We propose a log-weighted frequency (LWF) loss to better preserve fine details in reconstructed images.
- Extensive experiments demonstrate that our method surpasses SOTA methods in both burst denoising and novel view synthesis, while achieving faster inference.

2. Related Work

Neural Radiance Field. NeRF [30] models scenes via a continuous implicit function to predict emitted radiance and

volume density from a point’s coordinates and viewing angle. It shows remarkable success in the novel view synthesis (NVS) task, motivating numerous subsequent studies that aim to enhance reconstruction fidelity [1, 2, 16, 38], accelerate inference [9, 31, 35], or broaden its range of applications [5, 10, 33]. As an example, Pearl et al. [33] introduces Noise-Aware NeRF, which augments IBRNet [39] with additional noise-aware components to help reconstruct scene structures from noisy bursts of images. While these approaches yield promising results, NeRF-based methods still face significant limitations in both training and inference efficiency, primarily due to the heavy computational burden introduced by the volume rendering.

Gaussian Splatting. 3DGS [19] constructs explicit scene representations comprised of a vast number of Gaussian primitives. By adopting differentiable rasterization, it attains superior rendering speeds relative to NeRF-based methods, which are bottlenecked by computationally expensive volumetric rendering. Consequently, 3DGS has quickly gained popularity and found applications in various domains, including dynamic scene rendering [27, 40, 45], SLAM [18, 28, 44, 47], inverse rendering [17, 24, 42], digital humans [15, 21, 26], 3D content generation [23, 37, 46], and medical imaging [4, 48]. Traditional 3DGS methods typically require test-time optimization for each individual scene. In contrast, recent feed-forward models [7, 8, 43, 49] can reconstruct a scene in a single forward pass using as few as two images, thereby achieving significantly faster inference speeds. We leverage one of these models, GS-LRM [49], as our base model for burst denoising.

Burst Denoising. Early burst denoising techniques recover clean target images by predicting per-input-image per-pixel denoising kernels [29] or employing a Lucas-Kanade tracker to find a homography for each frame before denoising [14]. These methods yield promising results, but they can only deal with motions up to 2 pixels and show limited denoising capability. To address these issues, Xia et al. [41] uses larger denoising kernels to aggregate more spatial information. Bhat et al. [3] aligns each input image with the target images with optical flow and then denoises the images in a deep feature space. Dudhane et al. [12] proposes an edge-boosting feature alignment module and a pseudo-burst feature aggregation module. However, these 2D methods still lack 3D perception capabilities. Inspired by the success of 3D reconstruction techniques, researchers have started using 3D reconstruction models for burst denoising. Pearl et al. [33] extends the IBRNet [39] structure to handle noise. Tanay et al. [36] extends the multiplane image framework and introduces multiplane feature representation. Yet, these methods are either limited by high computational cost or by the capabilities of the 3D representation.

Novel View Synthesis in Degraded Scenes. While vanilla 3DGS [19] requires high-quality images as input,

degraded images are common in many real-world scenarios. Several Nerf- and 3DGS-based methods [13, 25, 33, 50, 51] synthesize novel view from degraded input images. Pearl et al. [33] proposed a noise-aware NeRF framework originally designed for burst denoising tasks, but is applicable to novel view synthesis from noisy input images. Rather than focus on 3D learning, NeRFLiX [51] and NeRFLiX++ [50] restore the rendered outputs with a postprocessing module Inter-Viewpoint Mixer. Recently, SRGS [13] was proposed to generate high-resolution renderings from low-resolution inputs using 3DGS. To this end, the method incorporates a pretrained 2D super-resolution model into its pipeline. HQGS [25] takes a different approach and improves the quality of the reconstructed point cloud by enhancing degraded inputs with high-frequency, edge-aware maps.

3. Problem Setup

Given a burst of noisy images, the task of burst denoising includes aggregating information from input images and then denoising one of them as the result. In this work, the target image to denoise is randomly chosen from the input images. We also choose to formulate the input as an unordered set rather than a sequential stream, primarily due to the potential motion and misalignment between consecutive frames.

Given that our model is built upon GS-LRM [49], a framework originally designed for novel view synthesis, it is natural to extend its capabilities to noisy conditions. Consequently, we further train and evaluate our method on the task of synthesizing novel views from noisy inputs.

Following the practice in KPN [29], we adopt a noise model that formulates the relationship between the noisy version and its clean linear counterpart as follows:

$$I_n(p) \sim \mathcal{N}(I_n^c(p), \sigma_r^2 + \sigma_s^2 I_n^c(p)), \quad (1)$$

where $I_n(p), I_n^c(p)$ refer to the intensity of the noisy and clean images at pixel p . σ_r and σ_s are noise parameters that depend on the sensor gain level (i.e., ISO). \mathcal{N} represents the Gaussian distribution. Following KPN [29], we evaluate our model over different gain levels of a sample camera. The relationship between gain levels and noise parameters σ_r, σ_s is illustrated in Fig. 2. We train our model in the high noise window (purple rectangle in Fig. 2) and evaluate our model on gain levels (black points in Fig. 2) up to 20.

4. Methods

Figure 3 illustrates the overall framework of our method. We begin by retraining GS-LRM [49] on our customized 3D noisy dataset RE10K-N as a simple baseline. The RE10K-N is adapted from the large-scale 3D dataset RE10K[52]. To enhance the quality of the reconstructed Gaussian point clouds, we then propose the Gaussian self-consistency (GSC) loss. Specifically, clean image bursts are simultaneously fed into the model during training to generate high-

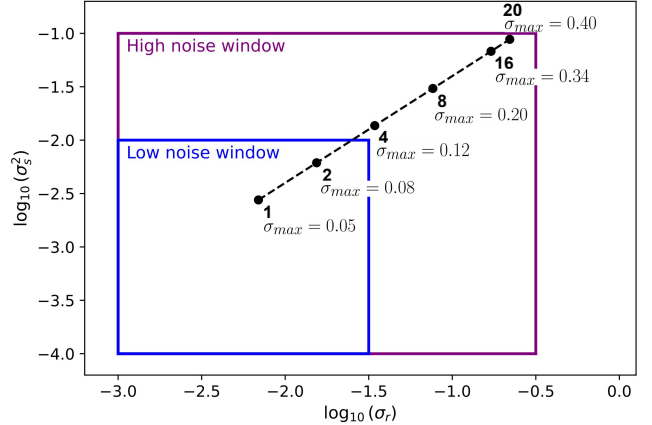


Figure 2. Noise parameters used during training and evaluation. Values (1-20) beside the point indicate gain levels defined in KPN [29]. $\sigma_{max} = \sqrt{\sigma_r^2 + \sigma_s^2}$ represents the maximum noise.

quality Gaussian point clouds. These point clouds then serve as 3D guidance for the point clouds reconstructed from the corresponding noisy bursts. Subsequently, to better capture relative depth and geometry, we replace the original Plücker rays [34] used in GS-LRM with the more effective reference-point Plücker coordinate (RPPC) [6]. Furthermore, we propose the log-weighted frequency (LWF) loss as supplementary frequency-level supervision, encouraging the model to preserve more high-frequency details.

4.1. A Simple Baseline

We build our model upon GS-LRM [49], a large reconstruction model for Gaussian splatting with strong spatial perception capability. We adopt GS-LRM as our baseline primarily because it is a feedforward 3DGS model that requires no per-scene optimization, enabling extremely fast inference. Moreover, it can reconstruct high-quality Gaussian point clouds from as few as two input images, demonstrating its strong reconstruction ability.

Simple Baseline. We retrain GS-LRM on the burst denoising task as a simple baseline. As illustrated in Fig. 3 (a), the multi-view inputs are first concatenated with camera conditions, and then are embedded and processed with standard Transformer blocks. Following the Transformer blocks, the network outputs per-pixel Gaussian parameters that define the 3D Gaussian point cloud. Specifically, each Gaussian G_p corresponding to pixel p is parameterized by a depth $d_p \in \mathbb{R}$, a scale $s_p \in \mathbb{R}^3$, a rotation quaternion $r_p \in \mathbb{R}^4$, an opacity $\alpha_p \in \mathbb{R}$, and an RGB color $c_p \in \mathbb{R}^3$. Given the camera origin \mathbf{o} and the ray direction \mathbf{d}_p of the pixel-aligned ray associated with pixel p , the 3D position of the Gaussian center is then computed as:

$$\boldsymbol{\mu}_p = \mathbf{o} + d_p \mathbf{d}_p. \quad (2)$$

As the final step, the reconstructed Gaussians are rendered through a standard differentiable 3DGS rasterization pipeline to produce images of target views.

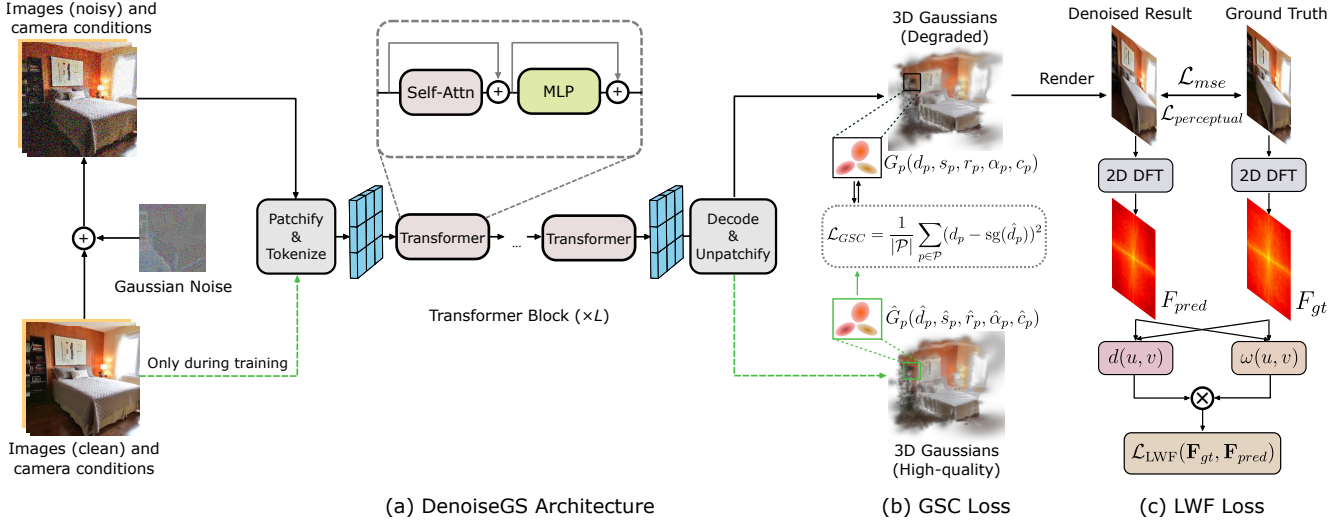


Figure 3. Pipeline. (a) Multi-view noisy inputs and camera conditions are processed by Transformer blocks to predict per-pixel Gaussian. During training, clean inputs are also fed into the model to generate high-quality Gaussian point clouds. (b) The high-quality point cloud is then used as guidance for the point cloud reconstructed from noisy inputs with our proposed Gaussian self-consistency loss. (c) The denoised result is further supervised in frequency domain with our proposed log-weighted frequency loss.

RE10K-N. Since GS-LRM tends to overfit when trained on the LLFF-N [33] dataset proposed in NAN, we construct a new dataset RE10K-N for training and evaluation based on the large-scale RealEstate10K (RE10K) dataset [52], which was used by GS-LRM [49]. Specifically, we take clean scene images from RE10K and synthesize noisy counterparts following the noise model defined in Eq. (1).

Before adding noise, as the model operates in the linear RGB space, we “linearize” the images from RE10K by reversing the gamma correction and applying inverse white balancing. After adding noise, instead of directly using the linearized images as inputs as in previous burst denoising methods [3, 29, 33, 41], we “delinearize” them back to sRGB and feed these processed images to the model. Since delinearization does not require any additional information, it does not compromise fairness in comparison.

Limitations of GS-LRM. The retrained GS-LRM achieves competitive performance. However, we observe two main limitations. **First**, since the final result is rendered from the reconstructed Gaussian point clouds, the quality of the point clouds critically affect the denoising results. However, as is shown in Fig. 4 (c) and Fig. 4 (d), the depth map predicted under noisy conditions differs greatly from the clean one, indicating point clouds tend to degrade under noisy conditions. **Second**, the denoised images exhibit noticeable loss of fine details, particularly at high gain levels.

In the following sections, we will present our methods designed to ameliorate these issues and enhance GS-LRM’s performance in point cloud quality and detail preservation.

4.2. Gaussian Self-Consistency Loss

Motivation. To enhance the quality of the generated Gaussian point clouds, a potential solution is to incorporate addi-

tional depth priors, as in DepthSplat [43]. However, this approach has two inherent limitations. First, it relies on an external pretrained depth estimation network to predict pixel-wise depth maps, inevitably introducing its bias into the training process. Second, as our model is trained solely for burst denoising instead of novel view synthesis, the depth maps rendered from Gaussian point clouds do not align with the true scene depth, as is illustrated in Fig. 4. The depth map predicted by GS-LRM in Fig. 4 (c) exhibits a pattern that differs notably from the scene depth in Fig. 4 (b). These patterns are learned to enhance visual quality from specific viewpoints rather than to recover accurate geometry. Therefore, forcing our model’s depth map to align with an externally predicted depth map per-pixel may impair the reconstruction capacity of the model.

Instead, we can take advantage of the model’s inherent ability to generalize across different noise levels. Since the model is trained with bursts of varying noise levels, it naturally learns to handle both noisy and clean inputs, and can predict higher-quality point clouds from clean inputs. Therefore, Gaussian point clouds reconstructed from clean bursts can serve as reliable supervision for those generated from noisy ones. This enables the model to refine the Gaussian point clouds without requiring external depth priors.

GSC Loss. Inspired by the above observations, we propose the Gaussian self-consistency loss. It regularizes the Gaussian point clouds predicted from noisy images with the model’s own predictions from clean inputs. Specifically, during training, we additionally feed clean images into the model to generate higher-quality Gaussian point clouds. These point clouds then serve as 3D guidance for those reconstructed from noisy images. Let the Gaussian

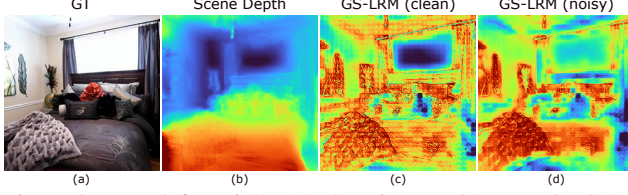


Figure 4. From left to right: (a) clean image; (b) scene depth (c) depth map predicted by GS-LRM on clean inputs; (d) depth map predicted by GS-LRM on noisy inputs.

point clouds predicted from noisy images be denoted as:

$$\mathcal{G} = \{G_p(d_p, s_p, r_p, \alpha_p, c_p) | p \in \mathcal{P}\}, \quad (3)$$

where \mathcal{P} denotes all the pixels in the input images and G_p denotes the Gaussian associated with the pixel p . Its depth, scale, rotation, opacity and color are denoted as $d_p \in \mathbb{R}$, $s_p \in \mathbb{R}^3$, $r_p \in \mathbb{R}^4$, $\alpha_p \in \mathbb{R}$, $c_p \in \mathbb{R}^3$. The Gaussian point clouds predicted from clean images is denoted as:

$$\mathcal{G}_{clean} = \{\hat{G}_p(\hat{d}_p, \hat{s}_p, \hat{r}_p, \hat{\alpha}_p, \hat{c}_p) | p \in \mathcal{P}\}. \quad (4)$$

As the model outputs per-pixel Gaussians, a natural one-to-one correspondence can be established between the Gaussians predicted from clean and noisy inputs. Based on this correspondence, we define the GSC Loss as the L2 loss between the depth attributes of these two Gaussian sets:

$$\mathcal{L}_{GSC}(\mathcal{G}, \mathcal{G}_{clean}) = \frac{1}{|\mathcal{P}|} \sum_{p \in \mathcal{P}} (d_p - \text{sg}(\hat{d}_p))^2, \quad (5)$$

where $|\mathcal{P}|$ denotes the number of pixels in the input images, which is also equal to the total number of the Gaussians. The $\text{sg}(\cdot)$ denotes the stop-gradient operation, which prevents gradients from flowing through the clean branch. The stop-gradient operation ensures that the model learns to make the Gaussian point clouds generated under noisy conditions approach those from clean conditions, rather than the other way around. It is worth noting that we only use the depth attribute in this loss, without involving other Gaussian properties. Our experiments show that adding multiple attributes to the loss may impair the training stability. Among these Gaussian attributes, depth is the most crucial factor for preserving the structure of the point cloud.

Warm-up Phase. To ensure the effectiveness of our GSC loss, it is crucial that the model is capable of reconstructing higher-quality Gaussians from clean images than from noisy ones — a condition not guaranteed at the early stage of training. Therefore, to ensure the guidance is meaningful, we introduce a warm-up phase, during which the GSC loss is not applied until the model reaches a sufficient reconstruction quality on clean inputs.

Reference-Point Plücker Coordinate. To provide the model with a more spatially informative camera condition, we adopt the RPPC proposed in [6] to replace the conventional Plücker ray representation. Existing approaches typically formulate pixel-aligned Plücker coordinates as $\mathbf{r} = (\mathbf{o} \times \mathbf{d}, \mathbf{d})$, with \mathbf{o} and \mathbf{d} representing the ray’s origin and direction, respectively. Nevertheless, the moment vector $\mathbf{o} \times \mathbf{d}$

primarily encodes angular information, which hinders the effective extraction of scene geometry and relative depth.

To address this, RPPC adopts a reference point located at the ray’s closest approach to the origin, instead of using the moment vector. Formally, this is expressed as:

$$\mathbf{r} = (\mathbf{o} - (\mathbf{o} \cdot \mathbf{d})\mathbf{d}, \mathbf{d}). \quad (6)$$

Compared to the standard Plücker coordinates, RPPC provides a more geometry-aware conditioning signal for the model, allowing it to better perceive the camera’s spatial conditions and more effectively interpret the 3D geometric relationships among multi-view inputs.

4.3. Log-Weighted Frequency Loss

To encourage the model to reconstruct high-frequency details more accurately, we employ a log-weighted frequency (LWF) loss in the frequency domain. Given the ground-truth and predicted images I_{gt} and I_{pred} , their discrete Fourier transforms are defined as:

$$\mathbf{F}_{gt}(u, v) = \sum_{h=0}^{H-1} \sum_{w=0}^{W-1} I_{gt}(h, w) e^{-j2\pi(\frac{uh}{H} + \frac{vw}{W})}, \quad (7)$$

$$\mathbf{F}_{pred}(u, v) = \sum_{h=0}^{H-1} \sum_{w=0}^{W-1} I_{pred}(h, w) e^{-j2\pi(\frac{uh}{H} + \frac{vw}{W})},$$

where $\mathbf{F}_{gt}, \mathbf{F}_{pred} \in \mathbb{R}^{H \times W \times C}$ are the frequency spectrum of all channels corresponding to I_{gt} and I_{pred} . The magnitude difference at frequency location (u, v) is given by

$$d(u, v) = \|\mathbf{F}_{gt}(u, v) - \mathbf{F}_{pred}(u, v)\|. \quad (8)$$

We then introduce a logarithmic weighting term:

$$\omega(u, v) = \log(\sqrt{d(u, v)} + 1), \quad (9)$$

which adaptively emphasizes harder frequency components with larger reconstruction errors. The final Log-weighted Frequency Loss is formulated as:

$$\mathcal{L}_{LWF}(\mathbf{F}_{gt}, \mathbf{F}_{pred}) = \frac{1}{HW} \sum_{u=0}^{H-1} \sum_{v=0}^{W-1} \omega(u, v) d(u, v). \quad (10)$$

This formulation balances the frequency-domain supervision by focusing more on challenging frequency regions while maintaining training stability.

4.4. Training Objective

Following GS-LRM, we adopt the Mean Squared Error (MSE) loss and the Perceptual loss in our training objective. In addition, we incorporate the Gaussian Self-Consistency (GSC) loss defined in Eq. (5) and the Log-weighted Frequency (LWF) loss defined in Eq. (10). Let I_{pred} denote the rendered target and I_{gt} denote the ground truth. The overall loss for our DenoiseGS is formulated as:

$$\begin{aligned} \mathcal{L} = & \lambda_{mse} \mathcal{L}_{MSE}(I_{pred}, I_{gt}) + \lambda_{lips} \mathcal{L}_{LIPS}(I_{pred}, I_{gt}) \\ & + \lambda_{gsc} \mathcal{L}_{GSC}(I_{pred}, I_{gt}) + \lambda_{freq} \mathcal{L}_{LWF}(I_{pred}, I_{gt}). \end{aligned} \quad (11)$$

Method	Inference Speed	Gain 1			Gain 2			Gain 4			Gain 8			Gain 16			Gain 20		
	FPS \uparrow	PSNR \uparrow	SSIM \uparrow	LPIPS \downarrow	PSNR \uparrow	SSIM \uparrow	LPIPS \downarrow	PSNR \uparrow	SSIM \uparrow	LPIPS \downarrow	PSNR \uparrow	SSIM \uparrow	LPIPS \downarrow	PSNR \uparrow	SSIM \uparrow	LPIPS \downarrow	PSNR \uparrow	SSIM \uparrow	LPIPS \downarrow
<i>Burst Denoising</i>																			
<i>2D Methods</i>																			
KPN [29]	140.85	36.82	0.965	0.078	34.61	0.948	0.112	32.27	0.920	0.159	29.68	0.875	0.226	26.81	0.803	0.318	25.84	0.772	0.353
BPN [41]	23.75	32.71	0.952	0.104	31.92	0.937	0.136	30.52	0.909	0.185	28.48	0.861	0.257	25.89	0.782	0.354	24.98	0.749	0.391
Deeprep [3]	20.49	37.18	0.968	0.059	35.92	0.958	0.070	33.80	0.937	0.097	31.11	0.898	0.145	28.18	0.839	0.216	27.23	0.815	0.243
<i>3D Methods</i>																			
NAN [33]	0.10	24.27	0.835	0.222	24.43	0.828	0.232	24.67	0.810	0.255	24.78	0.760	0.305	23.68	0.637	0.399	22.76	0.573	0.440
GS-LRM [49]	21.86	37.01	0.970	0.049	35.42	0.958	0.068	33.39	0.938	0.097	30.87	0.904	0.140	27.93	0.848	0.203	26.80	0.822	0.231
DenoiseGS	22.61	37.98	0.972	0.046	36.34	0.961	0.065	34.22	0.942	0.092	31.71	0.910	0.132	28.74	0.856	0.191	27.66	0.832	0.216
<i>Novel View Synthesis Under Noisy Conditions</i>																			
NAN [33]	0.10	23.56	0.773	0.260	23.74	0.769	0.267	24.04	0.758	0.284	24.37	0.723	0.320	23.79	0.624	0.394	23.08	0.571	0.429
GS-LRM [49]	21.86	25.34	0.839	0.146	25.24	0.834	0.154	25.02	0.825	0.170	24.55	0.804	0.198	23.59	0.763	0.249	23.10	0.742	0.273
DenoiseGS	22.61	25.97	0.854	0.134	25.86	0.849	0.142	25.62	0.839	0.158	25.12	0.818	0.185	24.14	0.779	0.234	23.64	0.760	0.254

Table 1. Quantitative results on RE10K-N dataset. Following NAN [33], we evaluate our model on two distinct tasks. For burst denoising, the target image is part of the input sequence, whereas for novel view synthesis under noisy conditions, the target is intentionally excluded. GS-LRM and DenoiseGS are evaluated with a burst size of 2, while other methods use a burst size of 8. To ensure the fairness of comparison, the 2-frame bursts are always selected as subsets of the corresponding 8-frame bursts for each scene.

5. Experiments

5.1. Experimental Settings

Dataset. We perform all of our main experiments on the RE10K-N dataset, with its generation process detailed in Sec. 4.1. Following prior work [7], we adopt the standard training and testing split for fair comparison.

Implementation Details. We implement DenoiseGS using the PyTorch framework [32] and train the model with the Adam optimizer [20] ($\beta_1 = 0.9$, $\beta_2 = 0.95$, and $\epsilon = 1 \times 10^{-8}$). To accelerate both the training and inference phases, we additionally incorporate Flash-Attention [11] from the xFormers library [22], following practice in GS-LRM [49]. We fix the burst size to 2, as recent work [7] has shown this setting is generally sufficient for scene reconstruction and can balance reconstruction quality and efficiency. Further analysis on this trade-off of burst size is detailed in Sec. 5.3. The loss weights in Eq. (11) are set to $\lambda_{mse} = 1.0$, $\lambda_{l_{ips}} = 0.5$, $\lambda_{gsc} = 0.06$, and $\lambda_{freq} = 1.75$. Our model is trained for 375k iterations on a single NVIDIA RTX A6000 GPU with images at 256×256 resolution. The GSC loss is applied after the first 120k iterations to stabilize the initial training and ensure the GSC loss provides a meaningful and consistent guidance. Following NAN [33], our model is trained on a high-noise range (highlighted with purple rectangle in Fig. 2) and evaluated across gain levels (black points in Fig. 2).

5.2. Comparison with Other Methods

Quantitative Comparison on Burst Denoising. We compare our method with a strong baseline (GS-LRM), state-of-the-art 2D methods (KPN [29], BPN [41], Deeprep [3]), and the leading 3D method (NAN [33]), with quantitative and qualitative results reported in Tab. 1. All competing baselines are retrained on our RE10K-N dataset over the high noise region (the purple rectangle in Fig. 2) to guarantee a fair comparison. It’s worth noting that our method achieves superior results using a burst size of only 2, whereas com-

petitors use 8, highlighting the efficiency of our approach. In terms of quantitative metrics (PSNR, SSIM, and LPIPS), our method consistently outperforms other baselines across all gain levels. Specifically, DenoiseGS is not only over $250\times$ faster than NAN—which struggles to scale effectively on large datasets—but also delivers substantially better restoration quality. It also surpasses the leading 2D methods in denoising performance while maintaining fast inference speeds comparable to BPN and Deeprep.

Qualitative Comparison on Burst Denoising. These metric improvements aligned with the visual comparisons in Fig. 5, where competing methods exhibit several common failure modes such as residual noise (NAN, BPN), over-smoothing of textured regions (Deeprep), or visual artifacts (GS-LRM). In contrast, since our DenoiseGS is trained under additional 3D-level guidance and supplementary frequency-domain supervision provided by our proposed GSC and LWF losses, it can generate clean results with fine details from inputs of high noise levels.

Quantitative Comparison on Novel View Synthesis. The quantitative results of novel view synthesis on RE10K-N are reported in Tab. 1. We compare our method with our baseline GS-LRM and NAN, and retrain all these models to conduct inference without receiving target image. Our DenoiseGS shows consistent improvement across noise levels.

Qualitative Comparison on Novel View Synthesis. Figure 6 illustrates the qualitative performance of our method on the NVS task. We observe that NAN and GS-LRM often struggle to synthesize high-quality novel views under noisy conditions. They either leave residual noise unrecovered, over-smooth the images, or easily produce floaters. In contrast, our method generate novel views free of noise with fewer floaters and noticeably sharper details.

5.3. Ablation Study

Break-down Ablation. In order to investigate the impact of specific design elements, we adopt the retrained GS-LRM

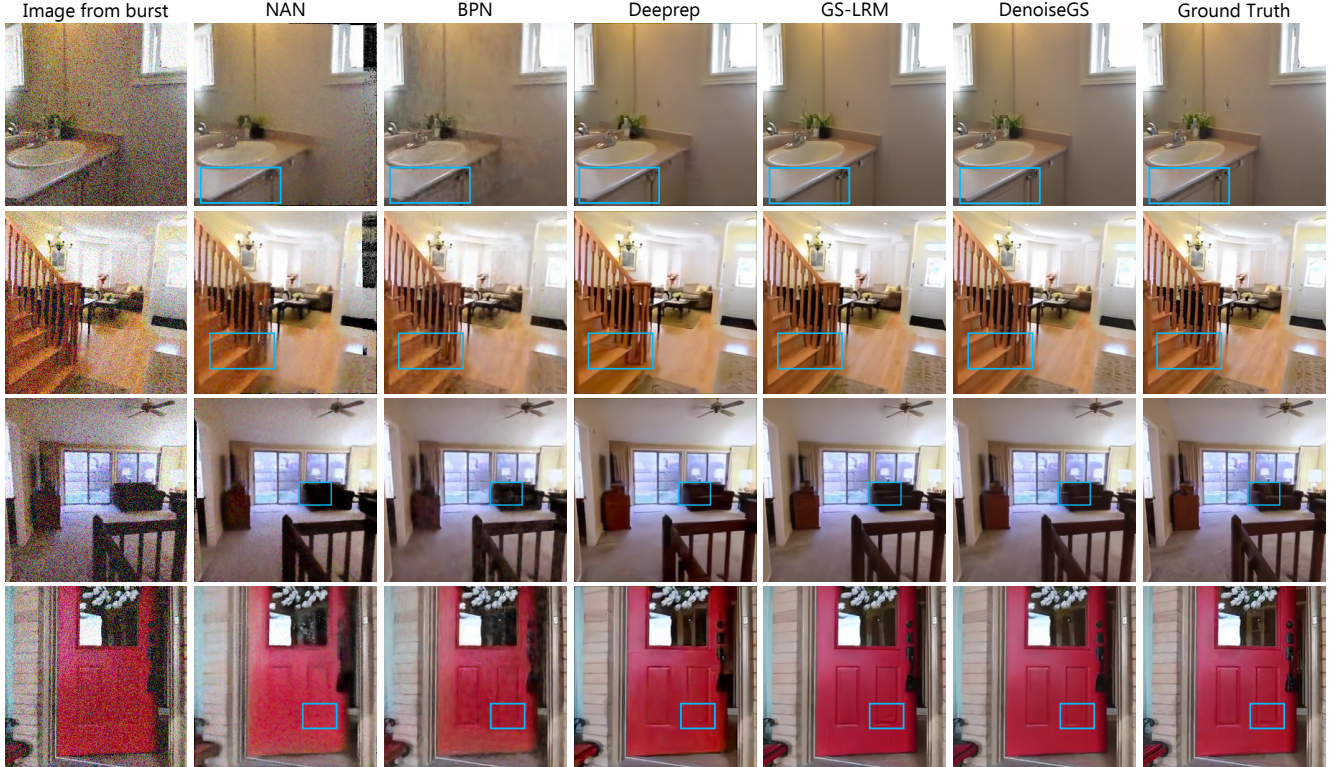


Figure 5. Qualitative comparison of burst denoising results on the RE10K-N dataset at gain 8. Key regions for comparison are highlighted with colored rectangles. While competing methods suffer from residual noise, over-smoothing, and visual artifacts, our approach robustly restores fine details and sharp structures from highly noisy inputs. Please zoom in for a better view.

GSC	Warmup	LWF	RPPC	PSNR \uparrow	SSIM \uparrow	LPIPS \downarrow	Depth \downarrow	Method	PSNR \uparrow	SSIM \uparrow	LPIPS \downarrow	
-	-	-	-	30.87	0.904	0.139	0.381	Gaussian Loss	31.39	0.907	0.138	
+	+	-	-	31.37	0.906	0.137	0.210	GSC Loss	31.37	0.906	0.137	
-	-	+	-	31.15	0.907	0.137	0.338	(b) Study on GSC Loss				
-	-	-	+	31.09	0.906	0.140	0.391	Burst Size	PSNR \uparrow	SSIM \uparrow	LPIPS \downarrow	FPS \uparrow
+	+	+	-	31.49	0.908	0.134	0.269	2	31.70	0.910	0.132	22.61
+	-	+	+	31.36	0.902	0.136	0.261	3	31.78	0.913	0.125	17.67
+	+	+	+	31.70	0.910	0.132	0.241	4	31.94	0.916	0.119	11.61

(a) Break-down ablation study

(c) Study on burst size

Table 2. Ablations on the RE10K-N dataset. All the ablation results are evaluated at gain 8. In the break-down study (a), the “Warmup” refers to the warm-up phase for GSC loss, and the depth error is the absolute relative error.

as a baseline and conduct ablation experiments. The results are reported in Tab. 2a. We further compute the absolute relative depth error with respect to the depth maps generated by GS-LRM on clean inputs to assess the improvement in the spatial structure of the reconstructed Gaussian point clouds. As shown in the results, each component consistently improves performance, with the GSC loss providing the most significant gain. The use of GSC loss also contributes to the drop in the depth error. However, using GSC loss without the warm-up phase leads to a slight drop in performance, indicating the necessity of the warm-up phase.

GSC Loss. We conduct experiments to compare our GSC Loss with an alternative Gaussian Loss that uses GS-LRM to provide 3D supervision. Specifically, we replace the

clean Gaussian point clouds in Eq. (4) with those generated by our retrained GS-LRM, treating them as ground-truth guidance during training. As shown in Tab. 2b, both approaches achieve comparable quantitative performance. However, our GSC Loss has a clear advantage in that it does not rely on any pretrained external model. It provides an intrinsic, self-consistent supervision signal generated within the same network, alleviating potential bias or domain gap.

Frequency Spectral Visualization. To demonstrate the advantages of our LWF loss in preserving high-frequency details, we visualize the 2D frequency spectra of the denoised results in Fig. 7. It can be seen from the first two rows that the spectra without frequency supervision exhibit numerous dark regions around the edges, indicating the loss of high-



Figure 6. Qualitative comparison of novel view synthesis results under noisy conditions on the RE10K-N dataset at gain 8. Key regions are highlighted with colored rectangles. It can be observed that our method achieves superior noise suppression with less floating artifacts.

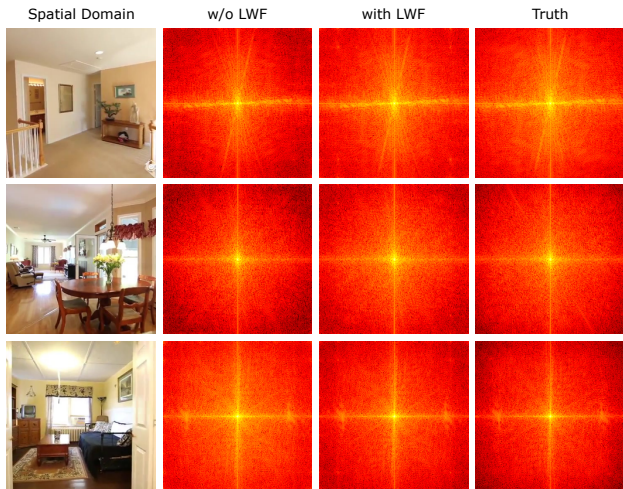


Figure 7. 2D frequency spectrum visualization with and without the LWF loss. The spectra in the first two rows correspond to the G channel, while the third row corresponds to the R channel.

frequency components, which will produce over-smooth artifacts in spatial domain. After applying LWF loss, these dark regions are effectively suppressed. Interestingly, as shown in the third row, we also observe that the model without LWF loss introduces spurious high-frequency components, leading to fake details in the denoised results. Our method suppresses such high-frequency components and thus produces results with more fidelity.

Burst Size. The burst size plays a crucial role in burst

denoising. Generally, a larger burst provides more complementary information for denoising the target image but at the cost of increasing the overall computational complexity. We evaluate our model under different burst sizes in Tab. 2c to analyze this trade-off. To effectively handle longer bursts, we fine-tune DenoiseGS for additional 100k steps with burst sizes of 3 and 4, respectively. As shown in the table, larger bursts consistently improve restoration quality across all metrics, particularly in LPIPS. However, this gain comes at the cost of slower inference, with FPS dropping from 22.61 to 11.61. Therefore, we adopt a burst size of 2 in practice to balance quality and efficiency.

6. Conclusion

In this paper, we present DenoiseGS, the first 3DGS-based framework for burst denoising and novel view synthesis under noisy conditions. To enhance the quality of Gaussian point clouds reconstructed from noisy inputs, we propose the GSC Loss. It regularizes degraded point clouds generated under noise with the model’s own predictions from clean inputs. To better preserve fine details, we further propose the LWF Loss, which emphasizes challenging high-frequency components and provides complementary frequency-domain supervision. Extensive experiments demonstrate that our method consistently outperforms state-of-the-art approaches in both burst denoising and novel view synthesis, while maintaining fast inference speed.

References

- [1] Jonathan T Barron, Ben Mildenhall, Matthew Tancik, Peter Hedman, Ricardo Martin-Brualla, and Pratul P Srinivasan. Mip-nerf: A multiscale representation for anti-aliasing neural radiance fields. In *ICCV*, 2021. 2
- [2] Jonathan T Barron, Ben Mildenhall, Dor Verbin, Pratul P Srinivasan, and Peter Hedman. Mip-nerf 360: Unbounded anti-aliased neural radiance fields. In *CVPR*, 2022. 2
- [3] Goutam Bhat, Martin Danelljan, Fisher Yu, Luc Van Gool, and Radu Timofte. Deep reparametrization of multi-frame super-resolution and denoising. In *ICCV*, 2021. 1, 2, 4, 6
- [4] Yuanhao Cai, Yixun Liang, Jiahao Wang, Angtian Wang, Yulun Zhang, Xiaokang Yang, Zongwei Zhou, and Alan Yuille. Radiative gaussian splatting for efficient x-ray novel view synthesis. In *ECCV*. Springer, 2024. 2
- [5] Yuanhao Cai, Jiahao Wang, Alan Yuille, Zongwei Zhou, and Angtian Wang. Structure-aware sparse-view x-ray 3d reconstruction. In *CVPR*, 2024. 2
- [6] Yuanhao Cai, He Zhang, Kai Zhang, Yixun Liang, Mengwei Ren, Fujun Luan, Qing Liu, Soo Ye Kim, Jianming Zhang, Zhifei Zhang, et al. Baking gaussian splatting into diffusion denoiser for fast and scalable single-stage image-to-3d generation and reconstruction. In *ICCV*, 2025. 3, 5
- [7] David Charatan, Sizhe Lester Li, Andrea Tagliasacchi, and Vincent Sitzmann. pixelsplat: 3d gaussian splats from image pairs for scalable generalizable 3d reconstruction. In *CVPR*, 2024. 1, 2, 6
- [8] Yuedong Chen, Haofei Xu, Chuanxia Zheng, Bohan Zhuang, Marc Pollefeys, Andreas Geiger, Tat-Jen Cham, and Jianfei Cai. Mvsplat: Efficient 3d gaussian splatting from sparse multi-view images. In *ECCV*. Springer, 2024. 1, 2
- [9] Zhiqin Chen, Thomas Funkhouser, Peter Hedman, and Andrea Tagliasacchi. Mobilenerf: Exploiting the polygon rasterization pipeline for efficient neural field rendering on mobile architectures. In *CVPR*, 2023. 2
- [10] Ziteng Cui, Lin Gu, Xiao Sun, Xianzheng Ma, Yu Qiao, and Tatsuya Harada. Aleth-nerf: Illumination adaptive nerf with concealing field assumption. In *AAAI*, 2024. 2
- [11] Tri Dao. Flashattention-2: Faster attention with better parallelism and work partitioning. *arXiv preprint arXiv:2307.08691*, 2023. 6
- [12] Akshay Dudhane, Syed Waqas Zamir, Salman Khan, Fahad Shahbaz Khan, and Ming-Hsuan Yang. Burst image restoration and enhancement. In *CVPR*, 2022. 1, 2
- [13] Xiang Feng, Yongbo He, Yubo Wang, Yan Yang, Wen Li, Yifei Chen, Zhenzhong Kuang, Jianping Fan, Yu Jun, et al. Srgs: Super-resolution 3d gaussian splatting. *arXiv preprint arXiv:2404.10318*, 2024. 3
- [14] Clément Godard, Kevin Matzen, and Matt Uyttendaele. Deep burst denoising. In *ECCV*, 2018. 2
- [15] Shoukang Hu, Tao Hu, and Ziwei Liu. Gauhuman: Articulated gaussian splatting from monocular human videos. In *CVPR*, 2024. 2
- [16] Wenbo Hu, Yuling Wang, Lin Ma, Bangbang Yang, Lin Gao, Xiao Liu, and Yuewen Ma. Tri-miprf: Tri-mip representation for efficient anti-aliasing neural radiance fields. In *ICCV*, 2023. 2
- [17] Yingwenqi Jiang, Jiadong Tu, Yuan Liu, Xifeng Gao, Xiaoxiao Long, Wenping Wang, and Yuexin Ma. Gaussianshader: 3d gaussian splatting with shading functions for reflective surfaces. In *CVPR*, 2024. 2
- [18] Nikhil Keetha, Jay Karhade, Krishna Murthy Jatavallabhula, Gengshan Yang, Sebastian Scherer, Deva Ramanan, and Jonathon Luiten. Splatam: Splat track & map 3d gaussians for dense rgb-d slam. In *CVPR*, 2024. 2
- [19] Bernhard Kerbl, Georgios Kopanas, Thomas Leimkühler, and George Drettakis. 3d gaussian splatting for real-time radiance field rendering. *ACM ToG*, 2023. 1, 2
- [20] Diederik P Kingma. Adam: A method for stochastic optimization. *arXiv preprint arXiv:1412.6980*, 2014. 6
- [21] Muhammed Kocabas, Jen-Hao Rick Chang, James Gabriel, Oncel Tuzel, and Anurag Ranjan. Hugs: Human gaussian splats. In *CVPR*, 2024. 2
- [22] Benjamin Lefaudeux, Francisco Massa, Diana Liskovich, Wenhan Xiong, Vittorio Caggiano, Sean Naren, Min Xu, Jieru Hu, Marta Tintore, Susan Zhang, et al. xformers: A modular and hackable transformer modelling library, 2022. 6
- [23] Yixun Liang, Xin Yang, Jiantao Lin, Haodong Li, Xiaogang Xu, and Yingcong Chen. Luciddreamer: Towards high-fidelity text-to-3d generation via interval score matching. In *CVPR*, 2024. 2
- [24] Zhihao Liang, Qi Zhang, Ying Feng, Ying Shan, and Kui Jia. Gs-ir: 3d gaussian splatting for inverse rendering. In *CVPR*, 2024. 2
- [25] Xin Lin, Shi Luo, Xiaojun Shan, Xiaoyu Zhou, Chao Ren, Lu Qi, Ming-Hsuan Yang, and Nuno Vasconcelos. Hggs: High-quality novel view synthesis with gaussian splatting in degraded scenes. In *ICLR*. 3
- [26] Xian Liu, Xiaohang Zhan, Jiaxiang Tang, Ying Shan, Gang Zeng, Dahua Lin, Xihui Liu, and Ziwei Liu. Humangaussian: Text-driven 3d human generation with gaussian splatting. In *CVPR*, 2024. 2
- [27] Jonathon Luiten, Georgios Kopanas, Bastian Leibe, and Deva Ramanan. Dynamic 3d gaussians: Tracking by persistent dynamic view synthesis. In *3DV. IEEE*, 2024. 2
- [28] Hidenobu Matsuki, Riku Murai, Paul HJ Kelly, and Andrew J Davison. Gaussian splatting slam. In *CVPR*, 2024. 2
- [29] Ben Mildenhall, Jonathan T Barron, Jiawen Chen, Dillon Sharlet, Ren Ng, and Robert Carroll. Burst denoising with kernel prediction networks. In *CVPR*, 2018. 2, 3, 4, 6
- [30] Ben Mildenhall, Pratul P Srinivasan, Matthew Tancik, Jonathan T Barron, Ravi Ramamoorthi, and Ren Ng. Nerf: Representing scenes as neural radiance fields for view synthesis. *Communications of the ACM*, 2021. 1, 2
- [31] Thomas Müller, Alex Evans, Christoph Schied, and Alexander Keller. Instant neural graphics primitives with a multiresolution hash encoding. *ACM ToG*, 2022. 2
- [32] Adam Paszke, Sam Gross, Francisco Massa, Adam Lerer, James Bradbury, Gregory Chanan, Trevor Killeen, Zeming Lin, Natalia Gimelshein, Luca Antiga, et al. Pytorch: An imperative style, high-performance deep learning library. *NeurIPS*, 2019. 6

- [33] Naama Pearl, Tali Treibitz, and Simon Korman. Nan: Noise-aware nerfs for burst-denoising. In *CVPR*, 2022. 1, 2, 3, 4, 6
- [34] Julius Plucker. Xvii. on a new geometry of space. *Philosophical Transactions of the Royal Society of London*, (155): 725–791, 1865. 3
- [35] Christian Reiser, Rick Szeliski, Dor Verbin, Pratul Srinivasan, Ben Mildenhall, Andreas Geiger, Jon Barron, and Peter Hedman. Merf: Memory-efficient radiance fields for real-time view synthesis in unbounded scenes. *ACM ToG*, 2023. 2
- [36] Thomas Tanay, Aleš Leonardis, and Matteo Maggioni. Efficient view synthesis and 3d-based multi-frame denoising with multiplane feature representations. In *CVPR*, 2023. 2
- [37] Jiayang Tang, Jiawei Ren, Hang Zhou, Ziwei Liu, and Gang Zeng. Dreamgaussian: Generative gaussian splatting for efficient 3d content creation. *arXiv preprint arXiv:2309.16653*, 2023. 2
- [38] Dor Verbin, Peter Hedman, Ben Mildenhall, Todd Zickler, Jonathan T Barron, and Pratul P Srinivasan. Ref-nerf: Structured view-dependent appearance for neural radiance fields. In *CVPR*. IEEE, 2022. 2
- [39] Qianqian Wang, Zhicheng Wang, Kyle Genova, Pratul P Srinivasan, Howard Zhou, Jonathan T Barron, Ricardo Martin-Brualla, Noah Snavely, and Thomas Funkhouser. Ibrnet: Learning multi-view image-based rendering. In *CVPR*, 2021. 1, 2
- [40] Guanjun Wu, Taoran Yi, Jiemin Fang, Lingxi Xie, Xiaopeng Zhang, Wei Wei, Wenyu Liu, Qi Tian, and Xinggang Wang. 4d gaussian splatting for real-time dynamic scene rendering. In *CVPR*, 2024. 2
- [41] Zhihao Xia, Federico Perazzi, Michaël Gharbi, Kalyan Sunkavalli, and Ayan Chakrabarti. Basis prediction networks for effective burst denoising with large kernels. In *CVPR*, 2020. 1, 2, 4, 6
- [42] Tianyi Xie, Zeshun Zong, Yuxing Qiu, Xuan Li, Yutao Feng, Yin Yang, and Chenfanfu Jiang. Physgaussian: Physics-integrated 3d gaussians for generative dynamics. In *CVPR*, 2024. 2
- [43] Haofei Xu, Songyou Peng, Fangjinhua Wang, Hermann Blum, Daniel Barath, Andreas Geiger, and Marc Pollefeys. Depthspat: Connecting gaussian splatting and depth. In *CVPR*, 2025. 2, 4
- [44] Chi Yan, Delin Qu, Dan Xu, Bin Zhao, Zhigang Wang, Dong Wang, and Xuelong Li. Gs-slam: Dense visual slam with 3d gaussian splatting. In *CVPR*, 2024. 2
- [45] Zeyu Yang, Hongye Yang, Zijie Pan, and Li Zhang. Real-time photorealistic dynamic scene representation and rendering with 4d gaussian splatting. *arXiv preprint arXiv:2310.10642*, 2023. 2
- [46] Taoran Yi, Jiemin Fang, Junjie Wang, Guanjun Wu, Lingxi Xie, Xiaopeng Zhang, Wenyu Liu, Qi Tian, and Xinggang Wang. Gaussiandreamer: Fast generation from text to 3d gaussians by bridging 2d and 3d diffusion models. In *CVPR*, 2024. 2
- [47] Vladimir Yugay, Yue Li, Theo Gevers, and Martin R Oswald. Gaussian-slam: Photo-realistic dense slam with gaussian splatting. *arXiv preprint arXiv:2312.10070*, 2023. 2
- [48] Ruyi Zha, Tao Jun Lin, Yuanhao Cai, Jiwen Cao, Yanhao Zhang, and Hongdong Li. R²-gaussian: Rectifying radiative gaussian splatting for tomographic reconstruction. *arXiv preprint arXiv:2405.20693*, 2024. 2
- [49] Kai Zhang, Sai Bi, Hao Tan, Yuanbo Xiangli, Nanxuan Zhao, Kalyan Sunkavalli, and Zexiang Xu. Gs-irm: Large reconstruction model for 3d gaussian splatting. In *ECCV*. Springer, 2024. 1, 2, 3, 4, 6
- [50] Kun Zhou, Wenbo Li, Nianjuan Jiang, Xiaoguang Han, and Jiangbo Lu. From nerflix to nerflix++: A general nerf-agnostic restorer paradigm. *TPAMI*, 2023. 3
- [51] Kun Zhou, Wenbo Li, Yi Wang, Tao Hu, Nianjuan Jiang, Xiaoguang Han, and Jiangbo Lu. Nerflix: High-quality neural view synthesis by learning a degradation-driven inter-viewpoint mixer. In *CVPR*, 2023. 3
- [52] Tinghui Zhou, Richard Tucker, John Flynn, Graham Fyffe, and Noah Snavely. Stereo magnification: Learning view synthesis using multiplane images. *arXiv preprint arXiv:1805.09817*, 2018. 3, 4